Computers and Structures 87 (2009) 1567–1579

Contents lists available at ScienceDirect

Computers and Structures

journal homepage: www.elsevier.com/locate/compstruc

Numerical modeling of electrochemical–mechanical interactions in lithium polymer batteries

Stephanie Golmon [a], Kurt Maute [a,*], Martin L. Dunn [b]

[a] Department of Aerospace Engineering, University of Colorado, Boulder, CO, United States
[b] Department of Mechanical Engineering, University of Colorado, Boulder, CO, United States

ARTICLE INFO

Article history:
Received 9 January 2009
Accepted 3 August 2009
Available online 5 September 2009

Keywords:
Multi-scale modeling
Finite element method
Homogenization
Porous electrode theory

ABSTRACT

This paper presents a multi-scale finite element approach for lithium batteries to study electrochemical–mechanical interaction phenomena at macro- and micro-scales. The battery model consists of a lithium foil anode, a separator, and a porous cathode that includes solid active materials and a liquid electrolyte. We develop a multi-scale approach to analyze the surface kinetics and electrochemical–mechanical phenomena within a single spherical particle of the active material. Homogenization techniques relate parameters in the micro-scale particle model to those in the macro-scale model describing the lithium ion transport, electric potentials and mechanical response based on porous electrode theory.

1. Introduction

Today, lithium batteries have the highest energy storage density of any secondary (rechargeable) battery technology [1]. However, their current use is limited to relatively low power applications such as cell phones and other small, portable electronics. Electrical systems requiring high voltages and/or currents such as battery packs in hybrid-electric vehicles still use traditional, heavy, lead-acid battery technology due to lower cost, longer lifetimes, and increased safety as failure in lithium batteries can be dramatic such as the laptop battery fires that occurred recently. Failure can be due to thermal runaway, internal shorting, and mechanical degradation of the electrodes. Lithium rechargeable batteries suffer in particular from a limited lifetime in comparison to other rechargeable chemistries, being limited to 100–150 charge–discharge cycles versus the 300 cycles achieved by other technologies [1]. This shortened lifecycle is due to deposits formed on the surface of the electrode during cycling [1], and possibly due to mechanical degradation of the electrode particles [2]. To understand the latter degradation phenomena, modeling and predicting the stresses in the electrode particles due to external mechanical loads and internal chemical processes is needed. The importance of understanding the interaction between chemical and mechanical phenomena in batteries is further highlighted when incorporating lithium batteries into structural composites to increase their storage-to-weight ratio. Such concepts have recently been advocated for aerospace systems dominated by weight constraints [3]. However, embedding a battery into a composite induces mechanical loads on the battery during manufacturing and operation.

In order to address the concerns of the relatively short lifecycle and safety problems in lithium batteries as well as to integrate batteries into structural composites, detailed understanding and mathematical modeling of the electrochemical and mechanical behavior and failure mechanisms of the batteries are needed. Balancing the trade-offs between structural and electrochemical performance is requisite in order to achieve these goals. To this end, in this paper we develop a coupled mathematical model of electrochemical and mechanical effects in lithium batteries.

The mechanisms causing capacity fade and failure of lithium batteries were studied by Wang et al. [2] who experimentally showed that capacity fade of lithium batteries after 60 cycles is linked to crack growth in the electrode. Wang et al. [4] found for $LiCoO_2$ cathodes that the active material particles are not uniformly strained during cycling and that the cycling can lead to fracture of the particles. Additional work on manganese cathodes has been performed by Thackeray et al. [5] and Aifantis and Hackney [6]. Several studies have focused on modeling the stress and crack formation in a single electrode particle. Huggins and Nix [7] developed a one-dimensional model to predict stresses and fracture in electrodes undergoing volume changes. Their model predicts a terminal particle size below which particles are not expected to crack. Aifantis and Dempsey [8] have modeled the crack formation in electrodes using facture mechanics. Christensen and Newman [9] predicted for a single spherical particle stress generation and

---

[*] Corresponding author. Address: Department of Aerospace Engineering Sciences, University of Colorado, CB 429, Boulder, CO 80301-0429, United States. Tel.: +1 303 735 2103; fax: +1 303 492 4990.

E-mail address: maute@colorado.edu (K. Maute).

0045-7949/$ - see front matter © 2009 Elsevier Ltd. All rights reserved.
doi:10.1016/j.compstruc.2009.08.005

fracture in lithium insertion compounds finding that particles are more likely to fracture when used in high-power applications. Christensen and Newman [10] also modeled the effects for a spherical particle of lithium manganese oxide, predicting that the intercalation-induced stress can exceed the strength of the particles. Aifantis et al. [11] used fracture mechanics to predict when an electrode particle will fracture, finding that smaller particles are preferable. Zhang et al. [12] studied intercalation-induced stress in $LiMn_2O_4$ particles, treating the intercalation-induced stress analogously to thermal stress and extending the spherical model to ellipsoidal particles.

Only few experimental studies incorporating batteries into structures and studying the effect of external mechanical loads have been performed. Thomas and Qidwai [3] have placed commercial lithium batteries in the wings of microair vehicles (MAV) resulting in improved range of the MAV. In their mechanical model of structurally integrated batteries, Thomas and Qidwai [3] assumed that the effects of electrochemical–mechanical interactions are negligible. Pereira et al. have studied experimentally the effects of flexural deflection [13] and uniaxial pressure [14] on lithium thin film batteries. Their observations suggest that up until structural failure of the battery, the electrochemical performance of the battery is not significantly affected by external mechanical loads. The same authors showed in a subsequent paper [15] that the same batteries could be successfully incorporated into a carbon fiber composite lay-up without degrading the battery performance and improving the mechanical properties of the composite. Much of the previous work on modeling lithium batteries has focused solely on electrochemical phenomena such as in the work of West et al. [16] and Doyle et al. [17] who model a porous electrode and in the work of Wang and Sastry [18] where the cathode microstructure is modeled. Garcia et al. [19,20] include mechanical effects in their model and study the performance of various nano-structured electrode layouts using dilute solution theory.

The goal of this study is to develop a numerical model to predict the electrochemical–mechanical interactions in structurally integrated lithium batteries subject to external mechanical loads, in order to understand and quantify the effects of electrochemical and mechanical parameters on performance and eventually, on failure mechanisms in these batteries. Resolving directly all length scales involved in the analysis of a battery, in particular modeling every cathode particle individually, leads to an impractical computational burden. Therefore, our approach is based on porous electrode theory and a multi-scale finite element formulation.

1.1. Electrochemical–mechanical interaction

When discharging a battery, electrons flow from the anode through an external electrical circuit and back to the cathode. The electric work done in the circuit leads to a drop in the electrical potential difference between the anode and cathode. A simple layout of a lithium battery includes a negative (anodic) current collector, a lithium foil anode, a gel or liquid electrolyte, a porous intercalation cathode, and a positive (cathodic) current collector. The external positive and negative terminals are connected to the current collectors. The cathode consists of two phases, a porous solid, active material and a liquid electrolyte that fills the pores. In the simplest case, the anode is a lithium foil while in modern batteries and secondary (rechargeable) batteries porous graphitic intercalation compounds are used as anode material systems. Research is ongoing to develop anodes with larger storage capacity. For the case of a porous anode, the anode is modeled the same way as the cathode. This model can be applied to any battery system that uses a single electrolyte. To structurally integrate the battery, it is sandwiched between two structural layers which results in an interlaminate stress applied to the battery. A representative configuration of a structurally integrated battery is depicted in Fig. 1.

When an external electrical load is applied, lithium (Li) is oxidized into Li^+ ions and electrons at the anode–separator interface, Γ_{AS}. The electrons flow through the current collector and the external circuit back to the positive current collector and into the cathode active material. Meanwhile, the Li^+ ions enter the solution phase of the separator and are carried by migration and diffusion across the separator–cathode interface, Γ_{SC}, to the cathode active material. At the surface of the active material particles, Li^+ ions are reduced and neutral Li diffuses into the cathode particles. To charge a secondary lithium battery, these processes reverse. As Li intercalates into the cathode active material particles, the particles swell resulting in both particle- and battery-level strains and stresses; for the Mn_2O_4 cathode discussed in this paper, the particles can swell up to 6.5% [12]. External mechanical loads also cause battery- and particle-level stresses and affect the uptake of Li by the particles in the cathode.

1.2. Proposed model

In this study we present a numerical approach for modeling the electrochemical–mechanical interactions in lithium batteries. To design and predict the performance of batteries subject to external

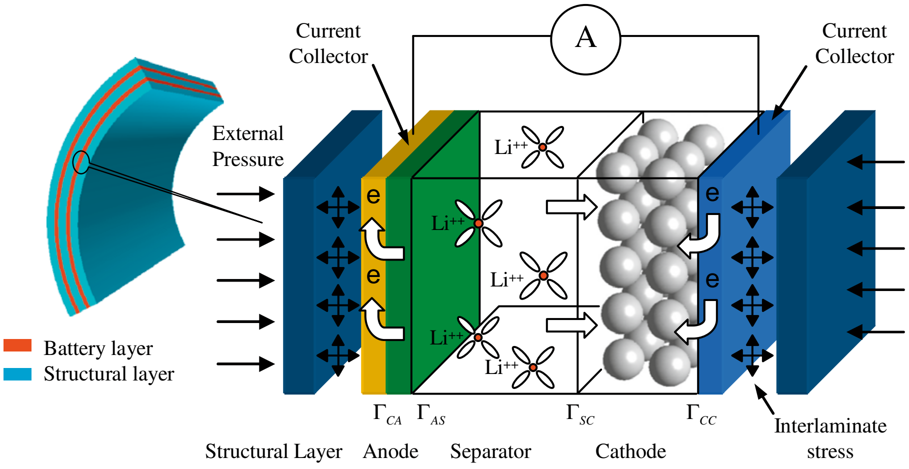

Fig. 1. Schematic of a structurally integrated lithium battery.

mechanical loads, our model accounts for the influence of electrochemical parameters such as discharge rate, liquid volume fraction in the cathode, active material particle size, and mechanical boundary conditions from the interlaminate stress, on both electrochemical and mechanical performance. This model predicts the effects of external loads and allows one to assessing the trade-offs between integration versus non-integration of the battery into a structural composite as well as suggest ways to improve overall battery design.

As the performance of lithium batteries involves multiple length scales, our approach is based on a multi-scale finite element formulation of the electrochemical–mechanical interactions. At the battery-level, or macro-scale, we model the Li^+ ion movement within the electrolyte and the resulting current and potential of the electrolyte, the potential of the solid cathode material, and the battery-level deformations. Within the cathode region, there are both solid active material and liquid electrolyte phases. Rather than modeling every individual cathode particle and the interactions between these particles, we analyze a representative single active material particle wherever information about the active material is needed in the macro-scale problem. We refer to this single particle model as the micro-scale. We model the lithium concentration throughout the particle, the stress state, and the displacements within the particle. Our numerical framework is based on an implicit Euler backward scheme and a Galerkin finite element model to discretize the macro- and micro-scale processes in time and space. Homogenization is used to relate the processes at the macro- and micro-scales.

The reminder of this paper is organized as follows: first we present a mathematical model of a lithium battery at multiple length scales and describe its numerical implementation for a one-dimensional macroscopic battery model. We verify our numerical framework by comparison with previous, experimentally verified, mathematical models. Lastly, we present results for the electrochemical and mechanical effects of varying the discharge current density, the active material particle radius, the volume fraction in the porous electrode, and the external mechanical boundary conditions due to interlaminate stress. For convenience, a list of all symbols used in this paper is provided in Appendix A.

2. Numerical modeling of batteries

Numerical models predicting the transport and reaction processes in batteries have been presented by Doyle et al. [17] who modeled the electrochemical phenomena using porous electrode theory and a finite-volume method. These models have shown good agreement with experimental discharge experiments but do not account for mechanical effects in the battery. Garcia et al. [19] developed a two-dimensional micro-scale model describing the mechanical effects of discharging and charging a battery based on dilute solution theory. The model is solved using a finite element scheme in space and a finite difference scheme in time. Initially, Garcia et al. [19] included only the separator and cathode; later Garcia and Chiang [20] extended this model and included an intercalation anode as well. Different nanostructures for the electrodes were investigated showing that the shorter the distance between the electrodes, the better the battery performs.

Wang and Sastry [18] developed a three-dimensional micro-scale model predicting the electrochemical performance of batteries with random and periodic micro-scale cathode layouts by modeling every cathode particle. Stress effects, both internal and external, are not included in this model. Zhang et al. [12] accounted for the effects of internal stresses due to lithium intercalation for single active material particles but ignore possible surface traction due to constraint by the surrounding aggregate in the electrode and/or due to external mechanical loads. They considered both spherical and ellipsoidal particles and showed that for spherical particles, larger particle size and discharge currents result in higher stress; and for ellipsoidal particles, large aspect ratios decrease the intercalation-induced stress for particles of a constant volume. Recently, Zhang et al. [21] extended their particle model to include heat generation during charge and discharge; resistive heating was found to be the most significant heat generation source at the particle-level.

2.1. Multi-scale modeling of structurally integrated batteries

The electrochemical and mechanical performance of Li batteries strongly depends on the interaction between macro-scale and micro-scale phenomena, in particular within the porous cathode. However, directly resolving all scales and modeling all particles in the cathode is not practical. Instead we incorporate the micro-scale effects into the macro-scale problem through homogenization approaches and constitutive models that are derived from homogenization methods. Three length scales can be distinguished: at the *macro-scale*, transport processes and mechanical deformations in the entire battery layer are modeled; at the *micro-scale*, a single active material particle in the cathode is modeled; and at the *meso-scale*, homogenization methods based on particle aggregates relate the micro- and macro-scales.

Our macro-scale model is based on porous electrode theory [22,23] and concentrated solution theory [22,23] predicting electrochemical processes in the separator and cathode. With porous electrode theory, the cathode is treated as a superposition of two continuous phases—the solid material including the active material, binders and conductive additives, and the pore-filling liquid electrolyte. The liquid volume fraction of the cathode is called the porosity, ε, $(\varepsilon = V_l/V)$. In the separator region of the battery there is no solid phase, so $\varepsilon = 1$. We extend the porous electrode theory to account for elastic and inelastic deformations due external loads and electrochemical eigenstrains. In this study, we do not model the structural layers surrounding the battery, and instead apply generic mechanical boundary conditions that with proper interpretation can be taken to represent the effect of the surrounding layers. We also assume that the lithium foil anode is perfectly rigid and therefore only model the separator and cathode regions. At the micro-scale, a single particle is modeled based on the work of Zhang et al. [12]. To relate the micro- and macro-scales, meso-scale homogenization methods are used.

The macroscopic response is characterized by the Li^+ ion concentration in the liquid phase, c_l, the electric potential of the liquid phase, ϕ_2, the electric potential of the solid phase, ϕ_1, and the macroscopic displacements, $\mathbf{u}$. The intercalation of Li^+ ions from the electrolyte into the particles is represented by an effective macroscopic pore wall flux, j_{eff}. The associated swelling of the particles results in a macroscopic electrochemical eigenstrain $\mathbf{e}^{ch}$.

At the micro-scale, a single representative active material particle is examined. The micro-scale variables include the microscopic lithium concentration in the particle, c_s, the microscopic displacements, u, and the hydrostatic stress field, σ_h. The rate of diffusion into the particle and subsequent particle swelling depends on the microscopic pore wall flux, j_s and the mechanical surface traction on the particle, P_s.

At the meso-scale, homogenization methods are used to relate the macroscopic and microscopic variables. The micro-scale pore wall flux, j_s, is dependent on the macro-scale variables, c_l, ϕ_1, and ϕ_2 and the micro-scale Li concentration at the particle surface, $c_{s,surf}$, through a micro-scale surface kinetics model. The micro-scale surface pressure exerted on the particle surface, P_s, is dependent on the macro-scale and micro-scale displacements, $\mathbf{u}$, and u through meso-scale homogenization of the mechanical variables.

The macro-scale effective pore wall flux, j_{eff}, is dependent on the micro-scale pore wall flux, j_s, through meso-scale homogenization of the electrochemical variables. The macro-scale chemically induced eigenstrain, $\mathbf{e}^{ch}$, is dependent on both the macro-scale displacement, $\mathbf{u}$, and micro-scale displacements, u through meso-scale homogenization of the mechanical variables. The interdependency between macro- and micro-scale variables is illustrated in Fig. 2. Note that the micro-scale boundary conditions for the micro-scale model depend on both macro- and micro-scale variables.

2.2. Macro-scale equations

The electrochemical transport of Li^+ ions through the electrolyte and the current carried by the solid and liquid phases are described by three equations:

$$\varepsilon\frac{\partial c_l}{\partial t}+\nabla\cdot\mathbf{N}+\frac{1}{F}\frac{\partial t_+^0}{\partial c_l}\mathbf{i}_2\cdot\nabla c_l-(1-t_+^0)j_{eff}=0 \tag{1}$$

$$\nabla\cdot\mathbf{i}_1+F\,j_{eff}=0 \tag{2}$$

$$\nabla\cdot\mathbf{i}_2-F\,j_{eff}=0 \tag{3}$$

with the following constitutive equations:

$$\mathbf{N}=-D_{eff}\nabla c_l \tag{4}$$

$$\mathbf{i}_1=-\lambda\nabla\phi_1 \tag{5}$$

$$\mathbf{i}_2=-\kappa_{eff}\left[\nabla\phi_2-\frac{RT}{F}(1-t_+^0)\nabla\ln c_l\right] \tag{6}$$

Eq. (1) describes the transport of Li^+ ions through the electrolyte with $\mathbf{N}$ being the Li^+ ion flux. Faraday's constant is denoted by F. The ions are carried by both migration and diffusion effects. This equation includes two source terms to account for the migration due to the current $\mathbf{i}_2$ carried by the electrolyte and for the effect of Li ions leaving the electrolyte and intercalating into the solid material. The transference number, t_+^0, is the percentage of the current in the solution carried by the Li^+ ion rather than the anions in solution; the transference number is in general a function of the lithium ion concentration, c_l. As Li^+ ions leave the electrolyte and enter the solid material, this creates an effective pore wall flux, j_{eff}. The currents $\mathbf{i}_1$ and $\mathbf{i}_2$ in the solid and liquid phases are governed by Eqs. (2) and (3) with source terms to account for the effects of Li entering and exiting the phases. In the solid phase, Ohm's law (5) relates the current and electric potential. In the liquid phase, the constitutive relationship is defined by a modified Ohm's law (6) that accounts for the effect of Li^+ ion concentration on the current. Within the cathode region, the effective electrolyte diffusivity and conductivity are reduced from their values when no solid is present. A homogenization approach (the Bruggeman relations) is used to model the transport properties in the porous electrode [23]:

$$D_{eff}=\varepsilon D_2 \tag{7}$$

$$\kappa_{eff}=\varepsilon^{3/2}\kappa_\infty \tag{8}$$

The above model was introduced by Doyle et al. [17]. We have reformulated their model in terms of field and constitutive equations in order to facilitate the numerical treatment of the model. To account for electrochemical–mechanical coupling phenomena, we extended this electrochemical model to include mechanical deformations:

$$\nabla\cdot\boldsymbol{\sigma}+\mathbf{b}=\mathbf{0} \tag{9}$$

assuming the following linear constitutive and kinematic relationships:

$$\boldsymbol{\sigma}=\mathbf{C}:(\mathbf{e}-\mathbf{e}_{ch}),\quad \mathbf{e}=\frac{1}{2}(\nabla\mathbf{u}+\nabla\mathbf{u}^T) \tag{10}$$

where $\boldsymbol{\sigma}$ is the macroscopic stress tensor, $\mathbf{b}$ the vector of body forces, $\mathbf{C}$ the elasticity tensor, $\mathbf{e}^{ch}$ the electrochemical eigenstrain tensor, and $\mathbf{e}$ the total macroscopic strain tensor due to the macroscopic displacements, $\mathbf{u}$.

We model a current-controlled (galvanostatic) discharge process. We assume that there are no resistive loses in the Li foil anode and therefore for every electron that leaves the anode, a Li^+ ion enters the electrolyte. At the anode–separator interface, Γ_{AS}, the anode is modeled through a boundary condition of an influx of Li^+ ions and the requirement that all the current be carried by the electrolyte. This results in Dirichlet boundary conditions on the current carried by the solid and liquid phases and a Neumann boundary condition on the Li^+ ion flux. A Galvanic process is assumed to relate the current discharged to the number of lithium atoms that disassociate at the boundary yielding the Li^+ ion flux. At the cathode–current collector interface, Γ_{CC}, lithium cannot leave the battery, so the Li^+ ion flux is zero, and the solid cathode material carries all the current. We model two mechanical configurations through an elastic model, which is either fixed at both ends or has an external pressure applied at the anode–separator interface, Γ_{AS}. These boundary conditions are summarized in Table 1.

We start our simulations assuming an initially uniform Li^+ concentration. The potential in the electrolyte is zero and the potential in the solid phase is the open circuit potential, U', which depends on the initial Li concentration in the active particles. The battery is initially undeformed. These initial conditions are summarized as follows:

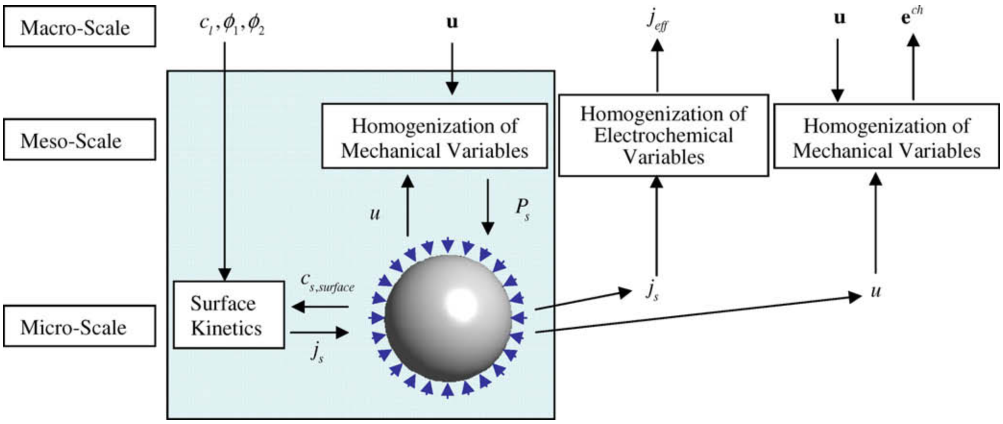

Fig. 2. Interdependency of macro- and micro-scales.

Table 1
Boundary conditions for macro-scale equations.

Boundary condition	Anode–separator interface Γ_{AS}	Cathode–current collector interface Γ_{CC}
Li$^+$ ion flux	$\mathbf{N} = \frac{I(1-t_+^0)}{F}$	$\nabla c_l = 0$
Current in solid particles	$\mathbf{i}_1 = \mathbf{0}$	$\mathbf{i}_1 = \mathbf{I}$
Current carried by electrolyte	$\mathbf{i}_2 = \mathbf{I}$	$\mathbf{i}_2 = \mathbf{0}$
Mechanical constraints	$\mathbf{u} = 0/\boldsymbol{\sigma} \cdot \mathbf{n} = \mathbf{p}_{lm}$	$\mathbf{u} = \mathbf{0}$

$$c_l = c_{l,0} \tag{11}$$

$$\phi_2 = 0 \tag{12}$$

$$\phi_1 = U'(c_{s,0}) \tag{13}$$

$$\mathbf{u} = 0 \tag{14}$$

where $c_{l,0}$ and $c_{s,0}$ are initial lithium concentrations in the liquid and solid phases.

2.3. Micro-scale equations

The micro-scale particle model is based on the work of Zhang et al. [12] where diffusion-induced stress in a particle is treated analogously to thermal stress. Zhang et al. solve the equations assuming zero surface traction on the particle and with a constant pore wall flux. In this study we place the particle within the cathode matrix. This requires accounting for particle–matrix and particle–particle interactions, both of which result in surface tractions. While the micro-scale governing equations presented subsequently are the same as in Zhang et al. [12], in our model the boundary conditions change significantly. Also, the pore wall flux into the cathode particles changes at different locations throughout the cathode and is modeled by the Butler–Volmer equation which depends on both micro- and macro-scale variables. The Butler–Volmer equation is widely used in electrochemistry to express the reaction kinetics at the particle surface as the difference between the cathodic and anodic currents [22,24].

The diffusion of Li within the particle is governed by [12]:

$$\frac{\partial c_s}{\partial t} + \nabla \cdot \mathbf{J} = 0 \tag{15}$$

and the static equilibrium for the particle in the absence of body forces is [12]:

$$\sigma_{ij,i} = 0 \tag{16}$$

with the following constitutive and kinematic equations [12,17]:

$$\mathbf{J} = -D_s\left(\nabla c_s - \frac{\Omega c_s}{RT}\nabla\sigma_h\right) \tag{17}$$

$$\sigma_h = (\sigma_{11} + \sigma_{22} + \sigma_{33})/3 \tag{18}$$

$$\sigma_{ij} = \frac{E}{1+\nu}\varepsilon_{ij} + \left(\frac{E\nu}{(1+\nu)(1-2\nu)}\varepsilon_{kk} - \frac{E\Omega}{2(1-2\nu)}c_s\right)\delta_{ij},$$
$$\varepsilon_{ij} = \frac{1}{2}\left(\frac{\partial u_i}{\partial x_j} + \frac{\partial u_j}{\partial x_i}\right) \tag{19}$$

Note that the Li$^+$ ion flux (17) only depends on the spatial gradient of the hydrostatic stress, $\nabla\sigma_h$, but not on the value of σ_h. The Li$^+$ ion flux at the particle surface is described by a Butler–Volmer model [17]:

$$BV(c_l, \phi_1, \phi_2, c_{s,surf}) - Fj_s = 0 \tag{20}$$

with

$$BV(c_l, \phi_1, \phi_2, c_s) = i_0\left[c_s \exp\left(\frac{\alpha_A F}{RT}(\eta - U'(c_s))\right) - (c_T - c_s)\exp\left(-\frac{\alpha_C F}{RT}(\eta - U'(c_s))\right)\right],$$
$$i_0 = Fk_2(c_{\max} - c_l)^{\alpha_C}(c_l)^{\alpha_A}, \quad \eta = \phi_1 - \phi_2 \tag{21}$$

The macro-scale response influences the micro-scale model through the boundary conditions at the particle surface. Stresses within the electrode come from two sources: inhomogeneous swelling of the cathode upon intercalation of lithium and from any applied external load. Micro- and macro-scale stresses are related via homogenization of the mechanical response; for this we use the Mori–Tanaka Theory [25] described in Section 2.4. At the macro-scale, the loads are propagated through the battery via Eq. (9). From the meso-scale homogenization procedure, the micro-scale mechanical surface pressure (23) exerted on the particle as a function of macro- and micro-scale displacements is calculated. Macro-scale electrochemical effects are felt by the micro-scale through the Butler–Volmer surface boundary condition (20). As the particle size is sufficiently small such that the macro-scale variables do not vary significantly over the size of a particle, we assume a uniform Li$^+$ ion flux and pressure at the surface of the particle:

$$\mathbf{J} = j_s \tag{22}$$

$$P_{ni} = \sigma_{ai}\hat{\mathbf{n}} \tag{23}$$

We further assume a uniform initial Li concentration, $c_{s,0}$, in the particle:

$$c_s = c_{s,0} \tag{24}$$

The micro-scale particle-level effects are related to the macro-scale through the homogenization methods described below.

2.4. Meso-scale homogenization methods

The microscopic pore wall flux is related to the macroscopic pore wall flux assuming a uniform flux for all particles in a unit volume of the cathode [23]:

$$j_{eff} = \frac{3(1-\varepsilon)}{R_s}j_s \tag{25}$$

Micro- and macro-scale mechanical properties are related using the Mori–Tanaka (M–T) effective-field theory [25]. This homogenization approach accounts for the interaction of spherical particles (solid phase) within a matrix host (liquid phase). It has been successfully used in a number of multiphysics settings where it has been shown to agree well with experiments for effective elastic properties [26], piezoelectric properties [27], thermal expansion [28], the macroscopic stress–strain curve with a plastically-deforming matrix [29], and estimates of internal stresses in individual particles [30]. Here we use the approach to generate estimates for the effective elastic properties and overall chemical eigenstrains of the aggregate as well as average stresses in the particles due to diffusion and mechanical loads. At the macro-scale, the effective elasticity tensor, $\mathbf{C}_{eff}$, for the cathode is given by [31,32]:

$$\mathbf{C}_{eff} = \mathbf{C}_m + (1-\varepsilon)(\mathbf{C}_s - \mathbf{C}_m)\mathbf{A}_s \tag{26}$$

with

$$\mathbf{A}_s = \mathbf{A}_D[\varepsilon\mathbf{I} + (1-\varepsilon)\mathbf{A}_D]^{-1} \tag{27}$$

$$\mathbf{A}_D = [\mathbf{I} + \mathbf{S}\mathbf{C}_m^{-1}(\mathbf{C}_s - \mathbf{C}_m)]^{-1} \tag{28}$$

where $\mathbf{C}_s$ and $\mathbf{C}_m$ are the stiffness matrices for the solid and liquid (matrix) phases, $\mathbf{I}$ is the identity matrix, and $\mathbf{S}$ is Eshelby's tensor, which is a function of the aspect ratio of the particle and the Poisson's ratio of the matrix phase.

Based on the M–T, model the surface pressure exerted on a spherical particle is a function of the macroscopic total strain, $\mathbf{e}$, and the macroscopic electrochemical eigenstrain, $\mathbf{e}^{ch}$ [31,32]:

$$\mathbf{P}_{ni} = (\mathbf{b}_s + \mathbf{B}_s\mathbf{C}_{eff}(\mathbf{e} - \mathbf{e}^{ch}))\hat{\mathbf{n}} \tag{29}$$

with

$$\mathbf{b}_s = (\mathbf{I} - \mathbf{B}_s)\left(\mathbf{C}_m^{-1} - \mathbf{C}_s^{-1}\right)\left(\mathbf{e}_s^{ch} - \mathbf{e}_m^{ch}\right) \tag{30}$$

$$\mathbf{B}_s = \mathbf{B}_D[\varepsilon\mathbf{I} + (1-\varepsilon)\mathbf{B}_D]^{-1} \tag{31}$$

$$\mathbf{B}_D = \mathbf{C}_s\left[\mathbf{I} + \mathbf{S}\mathbf{C}_m^{-1}(\mathbf{C}_s - \mathbf{C}_m)\right]^{-1}\mathbf{C}_m^{-1} \tag{32}$$

The macroscopic eigenstrain $\mathbf{e}^{ch}$ is computed as follows:

$$\mathbf{e}^{ch} = \mathbf{e}_m^{ch} + (1-\varepsilon)\left(\mathbf{e}_s^{ch} - \mathbf{e}_m^{ch}\right) + (1-\varepsilon)\left(\mathbf{C}_s^{-1} - \mathbf{C}_m^{-1}\right)\mathbf{b}_s \tag{33}$$

where $\mathbf{e}_m^{ch}$ and $\mathbf{e}_s^{ch}$ are the chemically induced strains in the matrix and solid phases. We calculate $\mathbf{e}_s^{ch}$ from the solution to the micro-scale problem and assume that there is no swelling of the matrix phase of the cathode due to the Li$^+$ ion concentration, i.e., $\mathbf{e}_m^{ch} = 0$. The macroscopic total strain, $\mathbf{e}$, is a function of the macroscopic displacements (10). Therefore, the stress exerted on the particle surface, P_{ni}, is a function of the total macroscopic strain and the microscopic strain of the particles. This interdependency results in a nonlinear model at the micro-scale with micro-scale boundary conditions on the surface pressure and pore wall flux both of which depend on the macro-scale properties.

3. Numerical implementation

Because the distance across the battery from the anode to the cathodic current collector is significantly smaller than the overall size of a typical battery, we idealize the problem to one-dimension. In our model, $x = 0$ corresponds to the anode–separator interface, Γ_{AS}, $x = \delta_s$ to the separator–cathode interface, Γ_{SC}, and $x = \delta_s + \delta_+$ to the cathode–current collector interface, Γ_{CC}. At the macro-scale, the idealization to one-dimension is straight-forward. At the micro-scale, the three-dimensional problem is idealized to one-dimension by assuming a spherical configuration and that the spatial variation of the macroscopic variables can be neglected locally at the micro-scale. The surface pressure exerted on the particle comes from the meso-scale homogenization, and the surface lithium flux is described by the Butler–Volmer equation.

At the macro-scale, we discretize Eqs. (1), (2), (3), and (9) in time by an implicit Euler backwards scheme and in space by a standard Galerkin finite element approach. The resulting discretized form of the macro-scale field equations is:

$$\begin{aligned}\mathbf{R}_{c_l}:\quad & \frac{1}{\Delta t}\int_\Omega N^T\varepsilon N(\hat{c}_l^{n+1} - \hat{c}_l^n)d\Omega \\ & + \int_\Omega \left(B^T\mathbf{N} + N^T\frac{1}{F}\frac{\partial t_+^0}{\partial c_l^{n+1}}N\hat{\mathbf{i}}_2 B\hat{c}_l^{n+1} - N^T(1 - t_+^0)Nj_{eff}\right)d\Omega \\ & + \left.\frac{I(1-t_+^0)}{F}\right|_{x=0} = \mathbf{0}\end{aligned} \tag{34}$$

$$\mathbf{R}_{i_1}:\quad \int_\Omega(-B^T\mathbf{i}_1^+N^TFN\hat{j}_{eff})d\Omega + \mathbf{I}|_{x=\delta_s+\delta_+} = \mathbf{0} \tag{35}$$

$$\mathbf{R}_{i_2}:\quad \int_\Omega(-B^T\mathbf{i}_2^-N^TFN\hat{j}_{eff})d\Omega + \mathbf{I}|_{x=0} = \mathbf{0} \tag{36}$$

$$\mathbf{R}_u:\quad \int_\Omega(-B^T\boldsymbol{\sigma} + N^TN\hat{\mathbf{b}})d\Omega + \mathbf{p}_{lm}|_{x=0} = \mathbf{0} \tag{37}$$

with:

$$\mathbf{N} = -D_{eff}B\hat{c}_l^{n+1} \tag{38}$$

$$\mathbf{i}_1 = -\lambda B\hat{\phi}_1^{n+1} \tag{39}$$

$$\mathbf{i}_2 = -\kappa_{eff}\left[B\hat{\phi}_2^{n+1} - \frac{RT}{F}(1 - t_+^0)\frac{1}{N\hat{c}_l^{n+1}}B\hat{c}_l^{n+1}\right] \tag{40}$$

$$\boldsymbol{\sigma} = \mathbf{C}_{eff}(\mathbf{e} - \mathbf{e}_{ch}), \quad \mathbf{e} = B\hat{\mathbf{u}}^{n+1} \tag{41}$$

where N is the shape function vector and B is the discretized differential operator. The integrals are evaluated by standard Gauss quadrature. The above equations are combined to yield the following dynamic residual equations:

$$\mathbf{R}_{dyn} = \frac{1}{\Delta t}\mathbf{M}\cdot(\hat{\mathbf{x}}^{n+1} - \hat{\mathbf{x}}^n) + \mathbf{R}(\hat{\mathbf{x}}^{n+1}) = 0 \tag{42}$$

where the vector $\hat{\mathbf{x}}$ collects all macroscopic state variables, $\hat{c}_l$, $\hat{\phi}_1$, $\hat{\phi}_2$, $\hat{\mathbf{u}}$, and the superscript n denotes the time increment. At each time step, Eq. (42) is solved by Newton's method. For the sake of numerical efficiency and robustness, we derive the Jacobian of the residual equations, $\mathbf{J}_{dyn}$, analytically. Because $\mathbf{e}_{ch}$ and j_{eff} depend on c_l, ϕ_1, ϕ_2, and $\mathbf{u}$, the Jacobian is fully populated and depends on the micro-scale state variables; the evaluation of $\mathbf{J}_{dyn}$ will be outlined later.

In order to compute the effective pore wall flux j_{eff} and the chemical eigenstrains $\mathbf{e}^{ch}$, at every Gauss point we solve a separate micro-scale problem for given values of the macroscopic variables. In this study, Eqs. (15) and (16) are solved assuming a spherical particle geometry. This assumption simplifies the micro-scale calculations to one-dimension. However, our computational framework could be easily augmented to treat particles of any shape. The continuous micro-scale equations for a spherical particle are given in spherical coordinates in Appendix B. Combining an Euler backward scheme and a Galerkin approach to discretize the micro-scale problem in time and space, the discretized governing equations in spherical coordinates are:

$$\begin{aligned}\mathbf{R}_{c_s}:\quad & \frac{1}{\Delta t}\int_r N^T4\pi(N\hat{r})^2N(\hat{c}_s^{n+1} - \hat{c}_s^n)dr \\ & + \int_r B^T4\pi(N\hat{r})^2\mathbf{J}dr - 4\pi R_s^2j_s|_{r=Rs} = \mathbf{0}\end{aligned} \tag{43}$$

$$\mathbf{R}_u:\quad \int_r(-B^T4\pi(N\hat{r})^2\sigma_r - N^T8\pi(N\hat{r})\sigma_t)dr + 4\pi R_s^2P_s|_{r=R_s} = \mathbf{0} \tag{44}$$

$$\mathbf{R}_{BV}:\quad BV\left(c_l^{n+1}, \phi_1^{n+1}, \phi_2^{n+1}, c_{s,surface}^{n+1}\right) - Fj_s = \mathbf{0} \tag{45}$$

with

$$\mathbf{J} = -D_s\left(B\hat{c}_s^{n+1} - \frac{\Omega}{RT}N\hat{c}_s^{n+1}B\hat{\sigma}_h^{n+1}\right) \tag{46}$$

$$\begin{aligned}\sigma_r &= \frac{E}{(1+v)(1-2v)}\left((1-v)B\hat{u}^{n+1} + 2v\frac{N\hat{u}^{n+1}}{N\hat{r}} - \frac{\Omega}{3}N\hat{c}_s^{n+1}(1+v)\right) \\ \sigma_t &= \frac{E}{(1+v)(1-2v)}\left(vB\hat{u}^{n+1} + \frac{N\hat{u}^{n+1}}{N\hat{r}} - \frac{\Omega}{3}N\hat{c}_s^{n+1}(1+v)\right)\end{aligned} \tag{47}$$

$$\begin{aligned}& BV\left(c_l^{n+1}, \phi_1^{n+1}, \phi_2^{n+1}, c_{s,surface}^{n+1}\right) \\ & \quad = i_0\left[Nc_{s,surface}^{n+1}\exp\left(\frac{\alpha_AF}{RT}\left(\eta - U'\left(N\hat{c}_{s,surface}^{n+1}\right)\right)\right)\right. \\ & \qquad \left. - \left(c_T - N\hat{c}_{s,surface}^{n+1}\right)\exp\left(-\frac{\alpha_CF}{RT}\left(\eta - U'\left(N\hat{c}_{s,surface}^{n+1}\right)\right)\right)\right], \\ & \quad i_0 = Fk_2\left(c_{\max} - c_l^{n+1}\right)^{\alpha_C}\left(c_l^{n+1}\right)^{\alpha_A}, \quad \eta = \phi_1^{n+1} - \phi_2^{n+1}\end{aligned} \tag{48}$$

where the radial position $r = 0$ is the center of the particle and $r = R_s$ is the particle surface. The macroscopic variables c_l, ϕ_1, and ϕ_2 defined at a Gauss point of the macro-scale model are considered constant within the micro-scale model. The micro-scale model is advanced in time synchronously with the macro-scale problem.

To simplify the numerical treatment of the nonlinear flux boundary conditions, we introduce the micro-scale pore wall flux, j_s, as an independent variable and consider the Butler–Volmer equation (45) as part of the governing equations. Furthermore, to limit the order of spatial derivatives in the diffusion equations (43) and (46) to first order, the hydrostatic stress is introduced as an independent field and the hydrostatic stress equation is satisfied in a weak sense:

$$R_{\sigma_h}: \quad \int_r \left(N^T 4\pi(N\hat{r})^2 N\hat{\sigma}_h^{n+1} - N^T 4\pi(N\hat{r})^2(\sigma_r + 2\sigma_t)/3\right)dr \tag{49}$$

To consistently approximate displacements and hydrostatic stress and to avoid numerical instabilities, the order of polynomial interpolation for the micro-scale displacements needs to be larger than for the hydrostatic stress. For this study, quadratic elements are used for the displacements and concentrations while linear elements are used for the hydrostatic stress interpolation.

The particle surface pressure depends on the macroscopic total strain and the microscopic volumetric strain through Eqs. (29)–(33). For spherical particles, the microscopic chemically induced eigenstrain of the solid particles, $\mathbf{e}_s^{ch}$, is equal to the volumetric strain of the solid particles, $\mathbf{e}_V$ which depends only on the displacement at the surface of the particle:

$$\mathbf{e}_V = \frac{1}{3}\left(\frac{\left(R_s + u_{surf}^{n+1}\right)^3}{R_s^3} - 1\right) \tag{50}$$

The homogenized macroscopic electrochemical eigenstrain $\mathbf{e}^{ch}$ is calculated from $\mathbf{e}_V$ using Eq. (33) with $\mathbf{e}_s^{ch} = \mathbf{e}_V$. The conversion from micro-scale pore wall flux j_s to the effective macro-scale flux j_{eff} is given by the homogenization model of Eq. (25).

For solving the nonlinear subproblems at each time step at the macro- and micro-scale, we use analytically derived Jacobians. In order to evaluate the macro-scale Jacobian, $\mathbf{J}_{dyn}$, the derivatives of the micro-scale variables j_s and $\mathbf{e}^{ch}$ with respect to the macro-scale state variables $c_l,\ \phi_1,\ \phi_2$, and $\mathbf{u}$ are required. The macroscopic variables $c_l,\ \phi_1$, and ϕ_2, are only present in the micro-scale model through the Butler–Volmer equation (20). The macroscopic displacements, $\mathbf{u}$, are only present in the boundary condition of the elastic residual (16) though the surface pressure. Differentiating the Butler–Volmer equation with respect to $c_l,\ \phi_1$, and ϕ_2 and the elastic residual with respect to $\mathbf{u}$, we can compute the required derivative of j_s with respect to the macroscopic variables. Details of this algorithm are given in Appendix C. The derivatives of electrochemical eigenstrain $\mathbf{e}^{ch}$ with respect to the macro-scale variables are slightly more involved and require the following expansion:

$$\frac{\partial \mathbf{e}_{ch}}{\partial n} = \frac{\partial \mathbf{e}_{ch}}{\partial \mathbf{e}_V}\frac{\partial \mathbf{e}_V}{\partial u_{surf}}\frac{\partial u_{surf}}{\partial n}, \quad \text{for } n = c_s, \phi_1, \phi_2 \tag{51}$$

$$\frac{\partial \mathbf{e}_{ch}}{\partial \mathbf{u}} = \frac{\partial \mathbf{e}_{ch}}{\partial \mathbf{e}_V}\frac{\partial \mathbf{e}_V}{\partial u_{surf}}\frac{\partial u_{surf}}{\partial \mathbf{u}} \tag{52}$$

The derivatives $\partial \mathbf{e}_{ch}/\partial \mathbf{e}_V$ and $\partial \mathbf{e}_V/\partial u_{surf}$ can be found by differentiating Eqs. (33) and (50), respectively. The evaluation of the derivatives of the displacements at the particle surface with respect to the macroscopic variables is given in Appendix C.

4. Verification

We verify our macro- and micro-scale models separately using published data. While our model is not specific for any particular material systems, for verification purposes we model a lithium foil anode, PEO—LiCF$_3$SO$_3$ electrolyte, and either a TiS$_2$ or Mn$_2$O$_4$ cathode active material. Other materials systems with binary electrolytes can be modeled given their electrochemical and mechanical properties. The material and geometric parameters along with the discretization parameters and convergence criteria used in the following simulations are given in Tables 2 and 3.

We verify our micro-scale problem by comparison with the results of Zhang et al. [12]. We compare our model for a single Mn$_2$O$_4$ particle of radius $R_s = 5\ \mu\text{m}$ with zero surface traction and a constant discharge current of $I = 10\ \text{A/m}^2$, which corresponds to a surface pore wall flux of $j_s = 10\ \text{A/m}^2/\text{F}$. The particle is discretized by 30 elements. Piecewise quadratic interpolations are used to approximate the lithium concentration and displacements and a piecewise linear interpolation is used for the hydrostatic stress. The evolution of the lithium concentration c_s in the particle is simulated for 1000 s with a time step $\Delta t = 25$ s.

Zhang et al. [12] compare their diffusion–stress coupling model (17) to the classical diffusion equation:

$$\mathbf{J} = -D_s \nabla c_s \tag{53}$$

They find that including the stress effect in Eq. (17) enhances the diffusion through the particle resulting in smaller Li concentration

Table 2
Material parameters.

Symbol	Value	Unit	Reference
PEO—LiCF$_3$SO$_3$ *electrolyte*			
$c_{l,\max}$	3920	mol/m^3	[17]
$c_{l,0}$	1000	mol/m^3	[17]
D_l	7.5×10^{-13}	m^2/s	[17]
κ_∞	6.5×10^{-3}	S/m	
t_+^0	$0.0107907 + 1.48837 \times 10^{-4}\ c_l$	–	[17]
$\partial t_+^0/\partial c_l$	1.48837×10^{-4}		[17]
TiS$_2$ *cathode*			
$c_{s,\max}$	29,000	mol/m^3	[17]
$c_{s,0}$	299	mol/m^3	[17]
D_s	5.0×10^{-13}	m^2/s	[17]
σ_s	10^4	S/m	[17]
Mn$_2$O$_4$ *cathode*			
$c_{s,\max}$	22,900	mol/m^3	[12]
$c_{s,0}$	4351	mol/m^3	[12]
D_s	7.08×10^{-15}	m^2/s	[12]
σ_s	10^4	S/m	
E	10^9	Pa	[12]
υ	0.3	–	[12]
Ω	3.497×10^{-6}	m^3/mol	[12]

Table 3
Geometric and discretization parameters and convergence criteria.

Symbol	Value	Unit	Reference
Nominal setup for PEO—LiCF$_3$SO$_3$, TiS$_2$ *system*			
R_s	5	μm	[17]
ε	0.3	–	[17]
I	12.1	A/m^2	[17]
Mechanical boundary condition	Fixed ends		
Nominal setup for PEO—LiCF$_3$SO$_3$, Mn$_2$O$_2$ *system*			
R_s	5	μm	[12]
ε	0.3	–	
I	12.1	A/m^2	
Mechanical boundary condition	Fixed ends		
Macro-scale problem			
Number of elements for separator			20
Number of elements for cathode			40
Newton convergence tolerance			1e−5
Micro-scale problem			
Number of elements			30
Newton convergence tolerance			1e−5

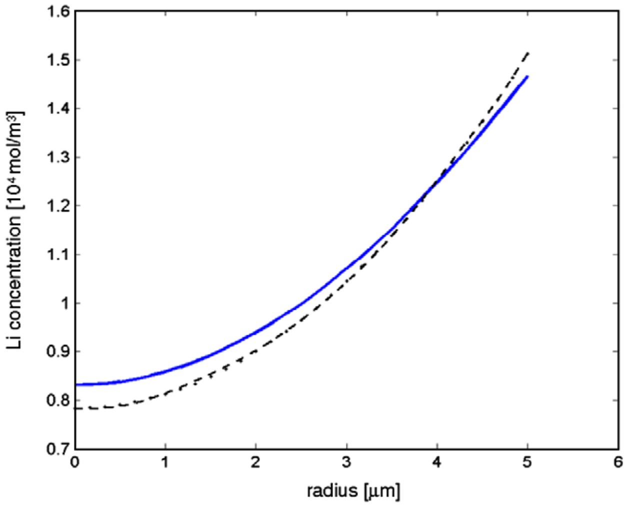

Fig. 3. Li concentration in a single particle at $t = 1000$ s; solid line: the stress-enhanced diffusion model; dashed line: classical diffusion model.

gradients. Our results, shown in Fig. 3, are indistinguishable from those of Zhang et al. [12].

To verify our macro-scale model, we compare our results with those of Doyle et al. [17] for a discharge current-controlled simulation of a one-dimensional battery model. The battery consists of a lithium foil anode, a separator of width $\delta_s = 50\ \mu\text{m}$, and a cathode of width $\delta_+ = 100\ \mu\text{m}$ and volume fraction $\varepsilon = 0.3$. The material system includes a PEO—$LiCF_3SO_3$ electrolyte and TiS_2 cathode particles with $R_s = 1\ \mu\text{m}$. The micro-scale diffusion of Li into the cathode particle is modeled by Eq. (53) and solved semi-analytically [17]. The separator is discretized by 20 and the cathode by 40 elements of uniform length. All macro-scale variables $c_l,\ \phi_1,\ \phi_2$, and $\mathbf{u}$ are approximated by piecewise linear interpolations. The time step ranges from $\Delta t = 1$ to 10s.

In Fig. 4, we plot the lithium concentration c_l over the normalized distance from the anode, $x/(\delta_s + \delta_+)$, at different instances in time. Overall our simulation results agree well with ones of Doyle et al. [17]. However in the first few seconds, the evolutions of the Li^+ ion concentration differ slightly as shown in Fig. 5. Our model predicts deeper levels of Li^+ ion depletion at the separator–cathode interface, Γ_{SC}. This discrepancy is due to differences in the numerical solution procedure. Doyle et al. [17] use a finite-volume approach and add artificial diffusion via an upwinding scheme to stabilize the results at the separator–cathode interface, Γ_{SC}. We do not observe any instability at this interface in our finite element formulation and therefore do not apply any artificial diffusion.

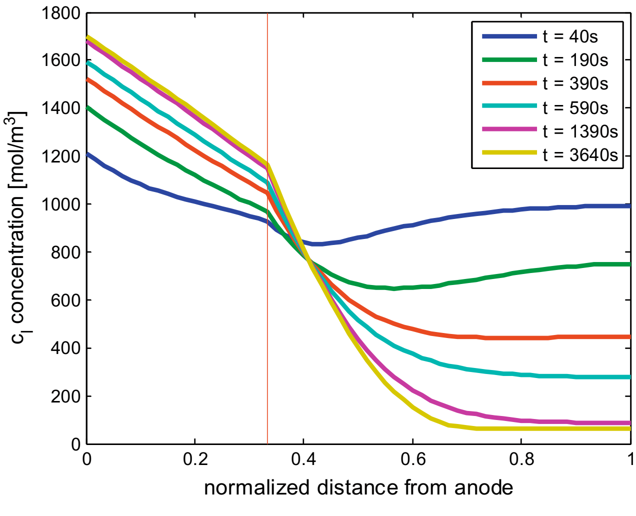

Fig. 4. Evolution of Li^+ concentration in electrolyte over time.

5. Numerical study of electrochemical–mechanical interaction phenomena

Our computational framework can be readily used to study electrochemical–mechanical interactions within the battery. To illustrate this capability, we revisit the one-dimensional battery model described above and simulate again a single current-controlled discharge process. Here we consider a different material system consisting of PEO—$LiCF_3SO_3$ electrolyte and Mn_2O_4 cathode. This particular material system is chosen due to the availability of material parameters; other systems can be modeled given the material properties. This cathode material system experiences a volume change of up to 6.5% upon lithium insertion [12]. The nominal setup for this system is summarized in Tables 2 and 3.

By varying the electrochemical parameters of the cathode particle radius, the porosity of the cathode, and the discharge current density, we study how the electrochemical properties affect both electrochemical and mechanical performance. Similarly, by changing the mechanical boundary conditions and applying external mechanical loads of different magnitudes, we study the influence of mechanical parameters on the battery performance. We can only partially verify our numerical studies due to a lack of published experimental and numerical studies on the effect of applied pressures on the battery performance.

5.1. Effect of discharge current density

Figs. 6 and 7 show the effects of different discharge current densities on the electrochemical performance of the battery. As expected, a higher current density leads to a lower utilization of the active material and therefore lower capacity. Utilization is the ratio of the actual over the maximum Li concentration that can intercalate into the active cathode material. In Fig. 6 we plot the potential difference between the battery electrodes versus the average utilization of the active cathode material. At higher current densities the voltage drops at lower utilizations, which is agreement with Doyle et al. [17], and results in higher Li concentration gradients in the cathode material, as seen in Fig. 7. At higher discharge rates the active material closest to the separator–cathode interface, Γ_{SC}, saturates with Li faster than the active material farther from the interface. At lower currents, the utilization across the cathode is more even.

Higher Li concentrations result in higher microscopic stresses. At any time step, the maximum radial stress in the spherical particles is always located at the center of the particle. Subsequently, we refer to the radial stress at the particle center as the peak radial stress. In Fig. 8, the maximum of the peak radial stress, which is the maximum over time of the peak radial stress, reached during discharge up to an average utilization of 0.3936 is plotted for different current densities. Larger discharge currents also result in greater maximum macroscopic electrochemical eigenstrains over time as seen in Fig. 9. Note the distributions of the macroscopic electrochemical eigenstrains follow the ones of the averaged Li concentration in the solid particles.

5.2. Effect of particle size

Motivated by increasing capabilities to synthesize engineered cathode materials, we study the effects of the particle size on the electrochemical and mechanical performance. Simulations with particle sizes ranging from 1 to 20 μm were performed. For this

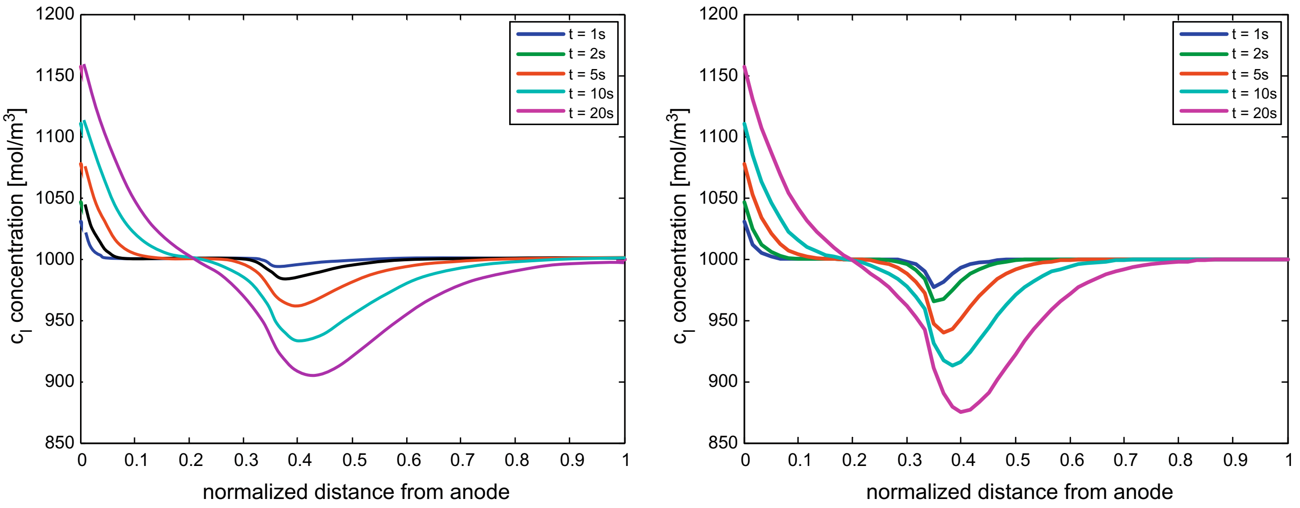

Fig. 5. Evolution of Li^+ concentration in electrolyte for $t \leqslant 20$ s; left: results of Doyle et al. [17]; right: results predicted by numerical framework presented in this paper.

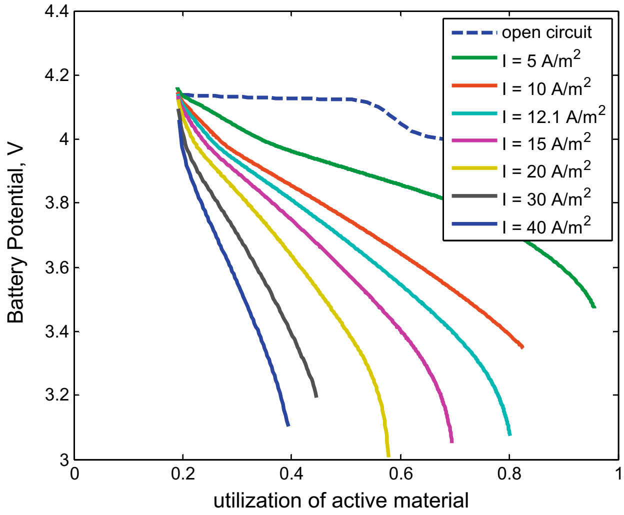

Fig. 6. Discharge characteristics for different discharge current densities.

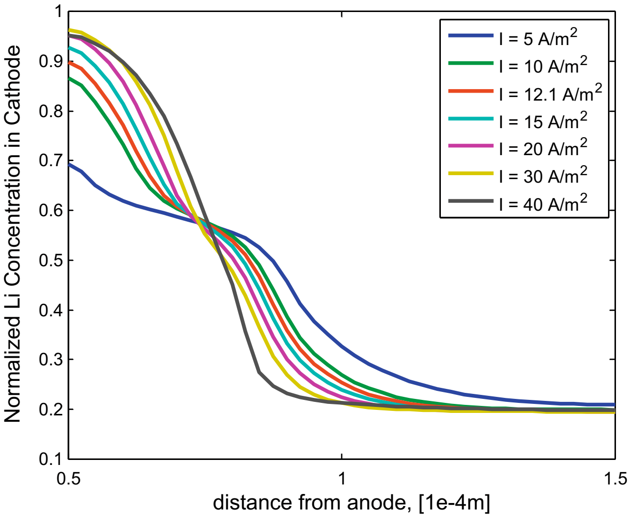

Fig. 7. Normalized lithium concentration profiles at average utilization of 0.3936.

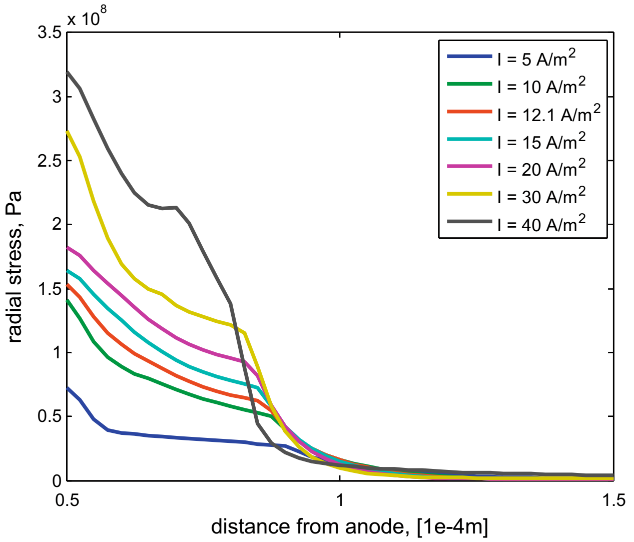

Fig. 8. Maximum peak radial stress in the particles over time when discharged from 0.19 to 0.3936 average utilization.

portion of the study, the volume fraction, ε, is kept constant at 0.3 and the particle size is varied, therefore the overall electrochemical capacity of the battery is unchanged. Our results show that smaller particle sizes give better electrochemical performance, characterized by the dependency of the battery voltage on the utilization of the solid cathode material, as shown in Fig. 10. Smaller particles also experience lower peak radial stresses over time, as shown in Fig. 11. This is in qualitative agreement with Wang and Sastry's simulations [18] which show a decrease in performance with larger particle sizes, and with Aifantis, Hackney, and Dempsey's work [11] which predicts that smaller particle sizes will be less susceptible to failure due to cracking.

5.3. Effect of porosity of the cathode

The porosity, ε, the liquid volume fraction in the cathode, affects the battery in terms of overall capacity and utilization of the active material. If the porosity is high, the energy capacity of the battery is lower because there is less active material into which Li can intercalate. In this case the active cathode material particles uptake

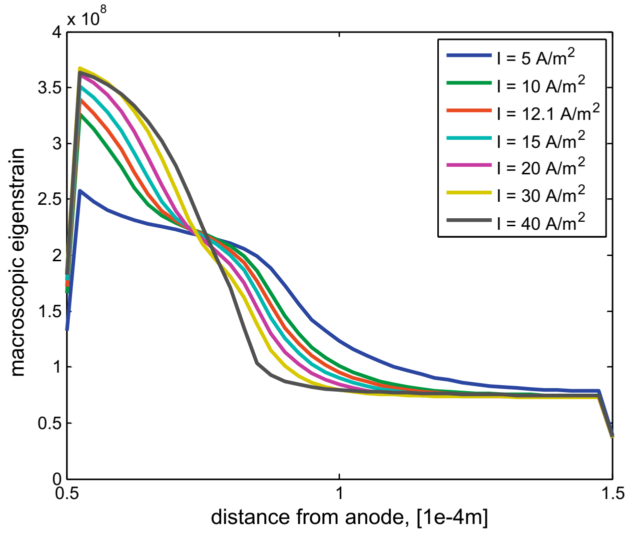

Fig. 9. Maximum macroscopic electrochemical eigenstrain over time in the cathode during discharge from 0.19 to 0.3936 average utilization.

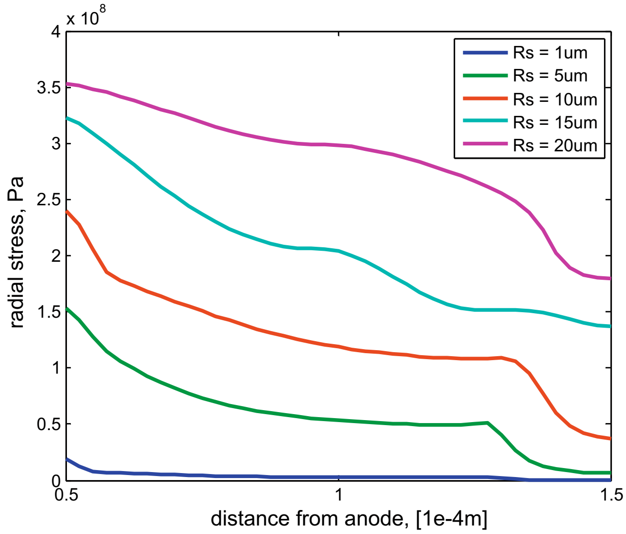

Fig. 11. Maximum peak radial stress in the cathode particles over time during discharge from 0.19 to 0.7 average utilization.

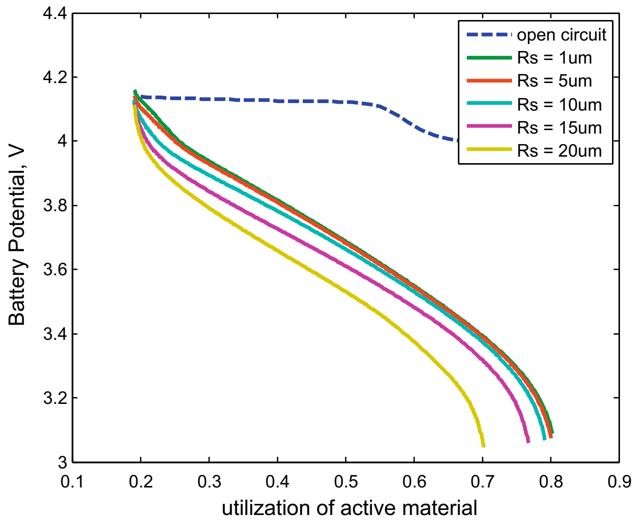

Fig. 10. Battery potential over utilization of cathode material for different particle sizes.

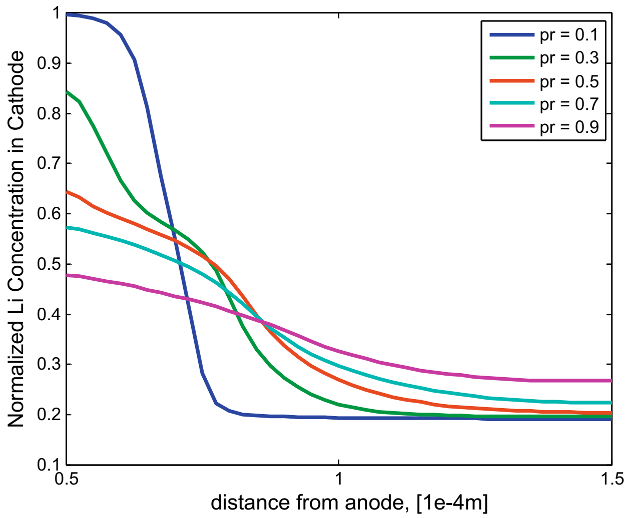

Fig. 12. Normalized Li concentration in cathode for different porosities at average utilization of the cathode material of 0.35.

Li^+ ions fairly evenly as seen in Fig. 12. However, if the porosity of the battery is too low, Li^+ ions do not effectively move through the liquid phase to the deeper regions of the cathode and higher gradients in Li concentration will be found across the cathode. In this case, the higher gradients prohibit full utilization of the cathode, so the increased theoretical capacity of the battery is not reached. The lower porosity also leads to higher macroscopic eigenstrains across the battery cathode as seen in Fig. 13.

5.4. Effect of mechanical boundary conditions

We compute the macro- and micro-scale response of our battery model for varying mechanical boundary conditions. We study two cases: (a) the battery is clamped at both ends, and (b) an external pressure is applied at the anode–separator interface, Γ_{AS}, and the cathode–current collector interface, Γ_{CC}, is clamped. Pressure values of ±10 MPa and ±100 MPa are considered.

In the case of spherical particles, our model predicts that there is no influence of the interlaminate stress on the electrochemical performance of the battery. As pointed out earlier, the micro-scale diffusion equation (17) depends only on the gradient of the hydrostatic stress. The predicted insensitivity of the electrochemical performance with respect to external mechanical loading conditions is in qualitative agreement with the experimental work of Periea et al. [15].

However, the dependency of macro- and micro-scale stresses across the battery on the mechanical boundary conditions cannot be ignored, as they will contribute to failure mechanisms in the battery. As is expected, greater interlaminate stress correlates to higher strains and stresses across the battery as seen in Figs. 14 and 15.

6. Conclusions

We have developed a multi-scale finite element model of the electrochemical and mechanical interactions in lithium batteries subject to external mechanical loads. At the macro-scale, we have extended Doyle and Newman's electrochemical porous electrode model to account for elastic deformations. At the micro-scale we have accounted for differences in Li^+ ion flux into the particles due to interfacial surface conditions using the Butler–Volmer

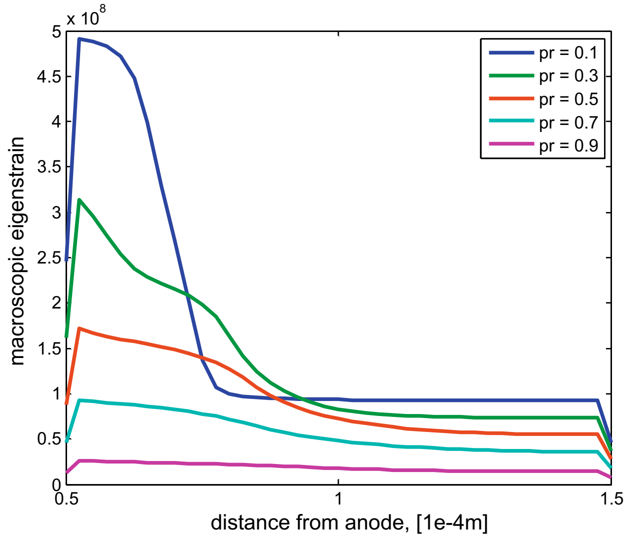

Fig. 13. Maximum macroscopic eigenstrain in the cathode over time when discharged from 0.19 to 0.35 average utilization.

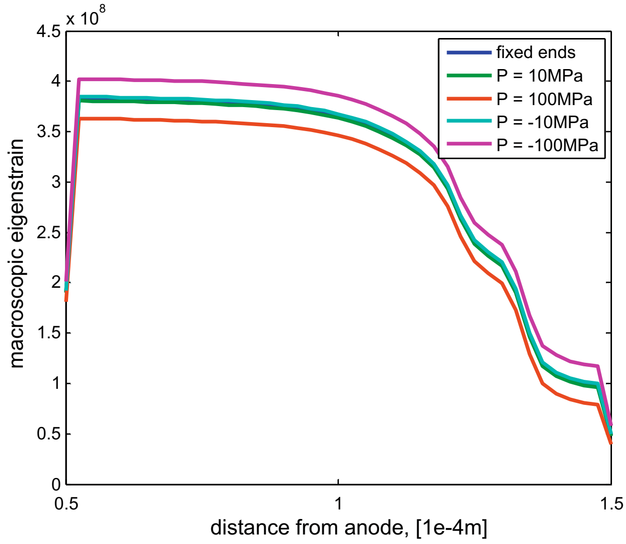

Fig. 14. Maximum macroscopic eigenstrain in cathode over time for different mechanical boundary conditions when discharged from 0.19 to 0.7 average utilization.

equation and for surface pressures exerted on the particles by the composite cathode matrix. We have introduced a meso-scale aggregate model to relate micro- and macro-scale mechanical effects. The macro- and micro-scale models are discretized in time by an implicit Euler backward scheme and in space by a Galerkin finite element method. The nonlinear macro- and micro-scale subproblems are solved by Newton's method using analytically derived Jacobians.

We have verified our macro- and micro-scale models separately through comparison with previously published simulation results. The potential of our multi-scale model was demonstrated by numerical studies on the influence of electrochemical and mechanical parameters on the battery performance. Our simulation results are in agreement with related simulation results and experimental studies, which predict better electrochemical performance and lower particle-level stresses for smaller cathode particle sizes [11,12], and no influence of mechanical boundary conditions on electrochemical performance [15].

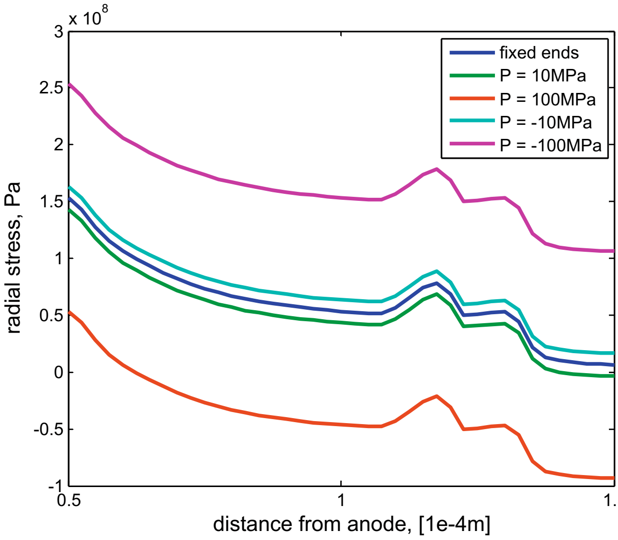

Fig. 15. Maximum peak radial stress in cathode particles over time, plotted over the cathode, when battery is discharged from 0.19 to 0.7 average utilization.

The numerical implementation and studies presented in this paper were limited to spherical cathode particles and single current-controlled discharge processes, neglecting accumulated stresses due to cycling of the battery. However, our numerical framework already allows the simulation of discharge–charge cycles and can be easily augmented to include more complex particle geometries. Currently, we are extending this framework to account for thermal effects at both macro- and micro-scale.

Acknowledgements

The authors gratefully acknowledge the support of the Air Force Office of Scientific Research MURI (grant F9550-06-1-0326) "Energy Harvesting and Storage Systems for Future Aerovehicles", monitored by Dr. B.L. Lee, and the support of the National Science Foundation under Grant CMMI 0729520. The first author acknowledges the support of the National Science foundation under the Graduate Research Fellowship Program. Any opinions, findings, and conclusions or recommendations expressed in this material are those of the authors and do not necessarily reflect the views of the Air Force Office of Scientific Research or the National Science Foundation.

Appendix A. List of symbols

Symbol	Units	Description
$A_s,\ B_s,\ b_s$		Concentration factors (Mori–Tanaka theory)
B	–	Derivatives of the shape function vector
$\mathbf{b}$	Pa	Body force
$\mathbf{C}$	Pa	Homogenized elasticity tensor
$\mathbf{C}_s,\ \mathbf{C}_m$	Pa	Isotropic elastic stiffness matrix for solid and liquid phases
c_l	mol/m^3	Concentration of lithium in electrolyte
$c_{\max}$	mol/m^3	Max concentration in polymer
c_s	mol/m^3	Concentration of lithium in solid particles

(*continued on next page*)

Appendix A. (*continued*)

Symbol	Units	Description
c_T	mol/m^3	Max concentration in solid
D_l	m^2/s	Diffusion coefficient of electrolyte
D_s	m^2/s	Diffusion coefficient of lithium in the solid
E	Pa	Young's modulus of solid particles
$\mathbf{e}$	–	Macroscopic strains due to macroscopic displacements
$\mathbf{e}^{ch}$	–	Chemically induced eigenstrain
$\mathbf{e}_V$	–	Volumetric strain of a particle
F	C/mol	Faraday's constant
I	A/m^2	Superficial current density
$\mathbf{i}_1$	A/m^2	Current density in solid phase
$\mathbf{i}_2$	A/m^2	Current density in liquid phase
j_{eff}	mol/m^2 s	Macro-scale effective pore wall flux
j_s	mol/m^2 s	Micro-scale pore wall flux
k_2	m^4/mol s	Reaction rate constant at cathode/polymer interface
$\mathbf{N}$	mol/m^2/s	Lithium ion flux in the electrolyte
N	–	Shape Function vector
P_s	Pa	Surface pressure exerted on a particle
$\mathbf{p}_{lm}$	Pa	Surface pressure
R	J/mol/K	Universal gas constant
R_s	m	Radius of cathode particles
r	m	Micro-scale distance from center of cathode particle
$\mathbf{S}$		Eshelby's tensor
T	K	Temperature
t	s	Time
t_+^0	–	Lithium ion transference number
U'	V	Open circuit potential
$\mathbf{u}$	m	Macroscopic displacements
u	m	Microscopic displacements within a particle
V	m^3	Total volume
V_l	m^3	Volume of liquid phase
x	m	Distance from anode
$\alpha_A,\ \alpha_C$	–	Anodic and cathodic transfer coefficients
δ_s	m	Thickness of separator
δ_+	m	Thickness of composite cathode
ε	–	Porosity, liquid volume fraction
ε_{ij}	–	Microscopic strain
ϕ_1	V	Potential in solid phase
ϕ_2	V	Potential in liquid phase
η	V	Surface overpotential
κ_{eff}	S/m	Effective conductivity of electrolyte
κ_∞	S/m	Conductivity of electrolyte, nothing else present
λ	S/m	Conductivity of solid matrix
ν	–	Poisson's ratio for solid particles
Ω	m^3/mol	Partial molar volume
Γ_{CA}		Current collector–anode interface
Γ_{AS}		Anode–separator interface
Γ_{SC}		Separator–cathode interface
Γ_{SC}		Cathode–current collector interface
$\boldsymbol{\sigma}$	Pa	Macroscopic stress
σ	Pa	Microscopic stress
σ_h	Pa	Hydrostatic stress

Appendix B. Micro-scale equations in spherical coordinates

We summarize the micro-scale equations in spherical coordinates which are used in our numerical implementation. The micro-scale governing equations are:

$$\frac{\partial c_s}{\partial t} + \left(\nabla_r + \frac{2}{r}\right)\mathbf{J} = 0 \tag{54}$$

$$\frac{d\sigma_r}{dr} + \frac{2}{r}(\sigma_r - \sigma_t) = 0 \tag{55}$$

$$\sigma_h - (\sigma_r + 2\sigma_t)/3 = 0 \tag{56}$$

with the corresponding constitutive equations:

$$\mathbf{J} = -D_s\left(\nabla_r c_s - \frac{\Omega c_s}{RT}\nabla_r \sigma_h\right) \tag{57}$$

$$\sigma_r = \frac{E}{(1+\nu)(1-2\nu)}\left((1-\nu)\nabla u + 2\nu\frac{u}{r} - \frac{\Omega}{3}\tilde{c}_s(1+\nu)\right) \tag{58}$$

$$\sigma_t = \frac{E}{(1+\nu)(1-2\nu)}\left(\frac{u}{r} + \nu\nabla u - \frac{\Omega}{3}\tilde{c}_s(1+\nu)\right) \tag{59}$$

The boundary conditions at the particle surface, $r = R_s$, are:

$$\mathbf{J} = j_s \tag{60}$$

$$\sigma_r = P_s \tag{61}$$

$$BV(c_l, \phi_1, \phi_2, c_{s,surf}) - Fj_s = 0 \tag{62}$$

where $BV(c_l, \phi_1, \phi_2, c_{s,surf})$ is defined as in Eq. (21). The boundary conditions at the particle center, $r = 0$, are:

$$\nabla_r c_s = 0 \tag{63}$$

$$u = 0 \tag{64}$$

Appendix C. Jacobian of micro-scale problem and derivatives of micro-scale variable with respect to macro-scale variables

The Jacobian of the micro-scale problem is simplified to show only variables describing surface phenomena and includes the following terms:

$$\mathbf{J} = \begin{bmatrix} \frac{\partial R_{c_s}}{\partial c_s} & 0 & \frac{\partial R_{c_s}}{\partial \sigma_h} & \frac{\partial R_{c_s}}{\partial j_s} \\ \frac{\partial R_u}{\partial c_s} & \frac{\partial R_u}{\partial u} & 0 & \frac{\partial R_u}{\partial j_s} \\ \frac{\partial R_{\sigma_h}}{\partial c_s} & \frac{\partial R_{\sigma_h}}{\partial u} & \frac{\partial R_{\sigma_h}}{\partial \sigma_h} & \frac{\partial R_{\sigma_h}}{\partial j_s} \\ \frac{\partial R_{BV}}{\partial c_s} & \frac{\partial R_{BV}}{\partial u} & \frac{\partial R_{BV}}{\partial \sigma_h} & \frac{\partial R_{BV}}{\partial j_s} \end{bmatrix} \tag{65}$$

In order to find values for the derivatives of the micro-scale variables with respect to macro-scale variables, $n = c_l,\ \phi_1,\ \phi_2$ and $\mathbf{u}$, the following systems of linear equations are solved:

$$\mathbf{J}\begin{bmatrix} \frac{\partial c_s}{\partial n} \\ \frac{\partial u_{surf}}{\partial n} \\ \frac{\partial \sigma_h}{\partial n} \\ \frac{\partial j_s}{\partial n} \end{bmatrix} = -\begin{bmatrix} 0 \\ 0 \\ 0 \\ \frac{\partial R_{BV}}{\partial n} \end{bmatrix} \tag{66}$$

$$\mathbf{J}\begin{bmatrix} \frac{\partial c_s}{\partial \mathbf{u}} \\ \frac{\partial u_{surf}}{\partial \mathbf{u}} \\ \frac{\partial \sigma_h}{\partial \mathbf{u}} \\ \frac{\partial j_s}{\partial \mathbf{u}} \end{bmatrix} = -\begin{bmatrix} 0 \\ \frac{\partial R_u}{\partial \mathbf{u}} \\ 0 \\ 0 \end{bmatrix} \tag{67}$$

where the derivatives $\partial R_{BV}/\partial n$ with $n = c_l,\ \phi_1,\ \phi_2$ and $\partial R_u/\partial \mathbf{u}$ are found analytically.

References

[1] Winter M, Brodd RJ. What are batteries, fuel cells, and supercapacitors? Chem Rev 2004;104(10):4245–69.

[2] Wang D et al. Cracking causing cyclic instability of $LiFePO_4$ cathode material. J Power Sources 2005;140(1):125–8.

[3] Thomas JP, Qidwai MA. The design and application of multifunctional structure-battery materials systems. JOM 2005;57(3):18–24.

[4] Wang H et al. TEM study of electrochemical cycling-induced damage and disorder in $LiCoO_2$ cathodes for rechargeable lithium batteries. J Electrochem Soc 1999;146(2):473–80.

[5] Thackeray MM et al. Advances in manganese-oxide composite electrodes for lithium-ion batteries. J Mater Chem 2005;15:2257–67.

[6] Aifantis KE, Hackney SA. An ideal elasticity problem for Li-batteries. J Mech Behav Mater 2003;14:413–27.

[7] Huggins RA, Nix WD. Decrepitation model for capacity loss during cycling of alloys in rechargeable electrochemical systems. Solid State Ionics 2000;6:57–63.

[8] Aifantis KE, Dempsey JP. Stable crack growth in nanostructured Li-batteries. J Power Sources 2005;143(1):203–11.

[9] Christensen J, Newman J. Stress generation and fracture in lithium insertion materials. J Solid State Electrochem 2006;10(5):293–319.

[10] Christensen J, Newman J. A mathematical model of stress generation and fracture in lithium manganese oxide. J Electrochem Soc 2006;153(6):1019–30.

[11] Aifantis KE, Hackney SA, Dempsey JP. Design criteria for nanostructured Li-ion batteries. J Power Sources 2007;165:874–9.

[12] Zhang X, Shyy W, Sastry AM. Numerical simulation of intercalation-induced stress in Li-ion battery electrode particles. J Electrochem Soc 2007;154(10):910–6.

[13] Pereira T et al. The performance of thin-film Li-ion batteries under flexural deflection. J Micromech Microeng 2006;16(12):2714–21.

[14] Pereira T et al. Performance of thin-film lithium energy cells under uniaxial pressure. Adv Eng Mater 2008;10(4):393–9.

[15] Pereira T et al. Embedding thin-film lithium energy cells in structural composites. Compos Sci Technol 2008;68(7–8):1935–41.

[16] West K, Jacobsen T, Atlung S. Modeling of porous insertion electrodes with liquid electrolyte. J Electrochem Soc 1982;129(7):1480–5.

[17] Doyle M, Fuller TF, Newman J. Modeling of galvanostatic charge and discharge of the lithium/polymer/insertion cell. J Electrochem Soc 1993;140(6):1526–33.

[18] Wang C, Sastry AM. Mesoscale modeling of a Li-ion polymer cell. J Electrochem Soc 2007;154(11):1035–47.

[19] Garcia RE et al. Microstructural modeling and design of rechargeable lithium-ion batteries. J Electrochem Soc 2005;152:255–63.

[20] Garcia RE, Chiang Y. Spatially resolved modeling of microstructurally complex battery architectures. J Electrochem Soc 2007;154(9):856–64.

[21] Zhang X, Sastry AM, Shyy W. Intercalation-induced stress and heat generation within single lithium-ion battery cathode particles. J Electrochem Soc 2008;155(7):542–52.

[22] Newman J, Thomas-Alyea KE. Electrochemical systems. Hoboken: Wiley; 2004.

[23] Doyle M. Design and simulation of lithium rechargeable batteries. PhD thesis, Department of Chemical Engineering, University of California, Berkeley; 1995.

[24] Bard AJ, Faulkner LR. Electrochemical methods. Hoboken: John Wiley and Sons; 2001.

[25] Mori T, Tanaka K. Average stress in matrix and average elastic energy of materials with misfitting inclusions. Acta Metall 1973;21:571–4.

[26] Dunn ML, Ledbetter H. Thermal expansion of textured polycrystalline aggregates. J Appl Phys 1995;78:1583–8.

[27] Dunn ML, Taya M. Micromechanics predictions of the effective electroelastic moduli of piezoelectric composites. Int J Solid Struct 1993;30:161–75.

[28] Dunn ML et al. Elastic constants of textured short fiber composites. J Mech Phys Solid 1996;44:1509–41.

[29] Dunn ML, Ledbetter H. Elastic–plastic behavior of textured short fiber composites. Acta Mater 1997;45:3327–40.

[30] Gall K et al. Internal stress storage in shape memory polymer nanocomposites. Appl Phys Lett 2004;85:290–2.

[31] Benveniste Y. A new approach to the application of Mori–Tanaka's theory in composite materials. Mech Mater 1987;6:147–57.

[32] Benveniste Y, Dvorak GJ. On a correspondence between mechanical and thermal effects in two-phase composites. Micromechancis and inhomogeneity. New York: Springer; 1990.